Available online at www.sciencedirect.com
ScienceDirect
Journal of Sound and Vibration 319 (2009) 885–903
JOURNAL OF SOUND AND VIBRATION
www.elsevier.com/locate/jsvi

Effect of tooth mesh stiffness asymmetric nonlinearity for drive and coast sides on hypoid gear dynamics

Jun Wang, Teik C. Lim*

Department of Mechanical Engineering, University of Cincinnati, 598 Rhodes Hall, P.O. Box 210072, Cincinnati, OH 45221, USA

Received 9 April 2007; received in revised form 14 June 2008; accepted 16 June 2008
Handling Editor: S. Bolton
Available online 18 July 2008

Abstract

A nonlinear time-varying dynamic model of a hypoid gear pair system with time-dependent nonlinear mesh stiffness, mesh damping and backlash properties is formulated to study the effect of mesh stiffness asymmetry for drive and coast sides on dynamic response. The asymmetric characteristic is the result of the inherent curvilinear tooth form and pinion offset in hypoid set. Using the proposed nonlinear time-varying dynamic model, effects of asymmetric mesh stiffness parameters that include mean mesh stiffness ratio, mesh stiffness variation and mesh stiffness phase angle on the dynamic mesh force response and tooth impact regions are examined systematically. Specifically, the dynamic models with only asymmetric mesh stiffness nonlinearity, with only backlash nonlinearity and with both asymmetric mesh stiffness and backlash nonlinearities are analyzed and compared. Using the parameters of a typical hypoid gear set, the extent of the effect of asymmetry in the mesh coupling on gear pair dynamics is quantified numerically. The results show that the increase in the mean mesh stiffness ratio tends to worsen the dynamic response amplitude, and the mesh stiffness parameters for drive side have more effect on dynamic response than those of the coast side one.

1. Introduction

Gear dynamics has been a subject of intense interest to the gearing community during the last few decades. The dynamic response in geared rotor systems due to the existence of gear transmission error excitation can be harmful to structures and also tend to generate highly annoying whines. Furthermore, gear possesses very rich dynamics due to the unique tooth-meshing characteristic that sets it apart from other power transmission devices.

One of the most sophisticated classes of gears is the hypoid set as illustrated in Fig. 1, which is designed to transmit rotational motion between two non-intersecting, perpendicular shafts. Unlike spur or helical gears, the line of action of a hypoid gear pair is not constant during the meshing process primarily due to the complex curvilinear features of the hypoid gear tooth geometry and kinematics. For the same reason, the mesh couplings in hypoid gears are not symmetric, that is their mesh parameters for the drive and coast sides are very different. A typical hypoid gear tooth form depicting the dissimilar features between drive and coast sides

*Corresponding author. Tel.: +1 513 556 4450; fax: +1 513 556 3390.
E-mail address: teik.lim@uc.edu (T.C. Lim).

0022-460X/$ - see front matter © 2008 Elsevier Ltd. All rights reserved.
doi:10.1016/j.jsv.2008.06.021

Nomenclature

b	gear backlash
c_i	mesh damping coefficient
e	unloaded static transmission error
f	nonlinear displacement function
g	nonlinear velocity function
I_p, I_g	mass moments of inertias of pinion and gear
$\vec{j}_l$	unit vector along pinion/gear rotating axis
k, k_i	mesh stiffness
m_e	equivalent mass
$\vec{n}_l$	unit normal vector at mesh point
p	difference between dynamic and static transmission error
$\vec{r}_l$	position vector of mesh point
S_I	coordinate system for dynamic formulation
t	time
T_p, T_g	mean loads applied to pinion and gear
δ	dynamic transmission error
λ_I	directional rotation radius
ω	excitation frequency
ζ	mesh damping ratio
η	system parameter
θ	rotational displacement
ϕ	phase angle

Subscripts

$a1$	fundamental harmonic
e	transmission error
k	mesh stiffness
l	label for pinion ($l=p$) and gear ($l=g$)
m	mean value
n	refer to natural mode
1	refer to drive side
2	refer to coast side

Superscripts

$\sim$	dimensionless quantities
$\rightarrow$	vector quantities
$'$	derivative with respect to time

is shown in Fig. 1(c). As a result, hypoid gear dynamics is not well documented, especially the asymmetric effect of mesh stiffness on dynamic response. In contrast, mesh characteristics of spur gears are essentially symmetric, and their dynamic models have been studied extensively [1–4]. Most of the previous studies on the dynamics of hypoid gear transmissions assume symmetric mesh parameters for simplicity. For example, an earlier study by Cheng and Lim [5], in spite of including backlash nonlinearity and time-varying mesh position and line-of-action vectors, considered only symmetric time-invariant mesh stiffness in their formulation. No prior study on the effect of hypoid gear mesh asymmetry on dynamic response is found in the open literature. Hence, one of the purposes of the current work is to address this gap in the literature.

A nonlinear, time-varying lumped parameter dynamic model of hypoid gear pair systems with asymmetric mesh stiffness and backlash nonlinearities is formulated analytically. Effects of asymmetric mesh stiffness parameters such as mean mesh stiffness ratio, mesh stiffness variation and mesh stiffness phase angle on the dynamic mesh force response and tooth impact regions are examined for the first time. Dynamic analysis applying the proposed models with asymmetric mesh stiffness nonlinearity only, backlash nonlinearity only and both nonlinearities are analyzed systematically to determine the severity and impact of the asymmetric behaviors.

2. Dynamic formulation

As shown in Fig. 1(a), a lumped parameter hypoid gear torsional vibration model that includes time-varying mesh point, line-of-action vectors, asymmetric mesh stiffness, mesh damping and backlash nonlinearity with unloaded static transmission error excitation is proposed for dynamic analysis. A single-point mesh model can be assumed here to represent the overall effect of gear meshing without significant loss of accuracy as we have applied the rigid lumped mass model for the gear bodies. It may be noted that the unloaded static transmission error is the deviation of the gear motion from ideal condition due to tooth profile errors and misalignments that are extremely difficult to avoid [6,7]. The mesh representation adopted in this study is basically a reduced order form derived from the results of a quasi-static tooth contact analysis [8]. The contact analysis generates

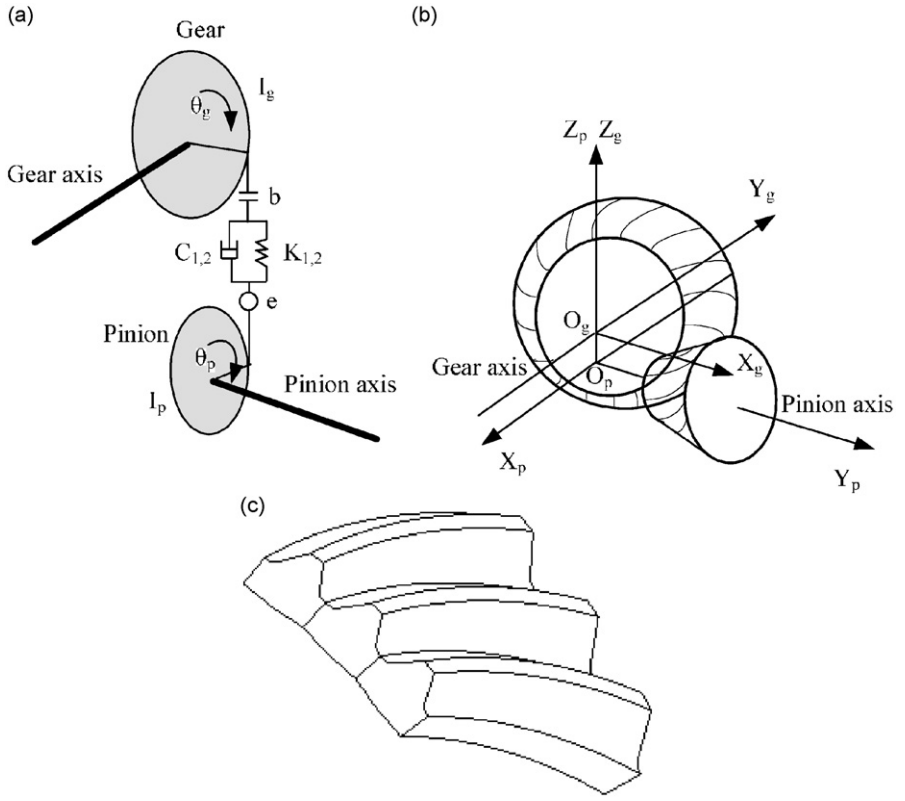

Fig. 1. (a) Hypoid gear pair model with two degrees of freedom, (b) pinion and gear coordinate systems and (c) a typical form of hypoid gear tooth geometry.

detailed geometrical, load and transmission error data at the surface profile of each tooth pair in engagement. Our mesh analysis technique uses the concept of contact cells to condense the tooth contact analysis results into the reduced order mesh representation applied in the proposed dynamic formulation. Details of the mathematical treatment of this approach have already been presented in a previous study related to the effects of time-varying mesh parameters and backlash on dynamic response [9]. The equations of motion of the two degrees of freedom (dof) dynamic model assumed for this study can be described as

$$I_p\ddot{\theta}_p + \lambda_p g(\dot{\delta} - \dot{e}) + \lambda_p f(\delta - e) = T_p, \tag{1a}$$

$$I_g\ddot{\theta}_g - \lambda_g g(\dot{\delta} - \dot{e}) - \lambda_g f(\delta - e) = -T_g, \tag{1b}$$

$$f(\delta - e) = \begin{cases} k_1(\delta - e - b), & \delta - e \geqslant b, \\ 0, & -b < \delta - e < b, \\ k_2(\delta - e + b), & \delta - e \leqslant -b, \end{cases} \tag{1c}$$

$$g(\dot{\delta} - \dot{e}) = \begin{cases} c_1(\dot{\delta} - \dot{e}), & \delta - e \geqslant b, \\ 0, & -b < \delta - e < b, \\ c_2(\dot{\delta} - \dot{e}), & \delta - e \leqslant -b, \end{cases} \tag{1d}$$

where I_p and I_g are the mass moments of inertias of pinion and gear, T_p and T_g are the mean loads applied on pinion and gear, e is unloaded static transmission error, $2b$ is the gear backlash, and k_1, c_1 and k_2, c_2 are the mesh stiffnesses and damping for drive and coast sides, respectively. Here, the mesh stiffnesses depict both nonlinear and time-varying characteristics. The deviation of gear motion from ideal state in dynamics or more

commonly known as the dynamic transmission error can be defined as

$$\delta = \lambda_p \theta_p - \lambda_g \theta_g, \tag{2}$$

while the directional rotation radius is given by

$$\lambda_l = \vec{n}_l \cdot (\vec{r}_l \times \vec{j}_l). \tag{3}$$

Here, $\vec{n}_l$ is the unit normal vector at the mesh point on the gear surface in the coordinate system S_l as shown in Fig. 1(b) ($l = p$, g for pinion and gear, respectively), $\vec{r}_l$ ($l = p,g$) is the position vector of mesh point and $\vec{j}_l$ ($l = p$, g) is the unit vector along the rotating axes of pinion and gear.

Suppose $p = \delta - e$, Eqs. (1a) and (1b) can be reduced to a single dof equation. Here, even though λ_l is time dependent, but since it is small and only vary slowly with time, and the average mesh point is typically continuous without significant abrupt change, it is reasonable to assume λ_l as time invariant ($\dot{\lambda}_l = \ddot{\lambda}_l = 0$) in the derivation. This assumption makes it possible to obtain the definite form. In the subsequent analysis λ_l is still considered as time varying. The definite form is given by

$$m_e \ddot{p} + g(\dot{p}) + f(p) = m_e \left(\frac{\lambda_p T_p}{I_p} + \frac{\lambda_g T_g}{I_g} - \ddot{e} \right), \tag{4a}$$

$$f(p) = \begin{cases} k_1(p-b), & p \geqslant b, \\ 0, & -b < p < b, \\ k_2(p+b), & p \leqslant -b, \end{cases} \tag{4b}$$

$$g(\dot{p}) = \begin{cases} c_1 \dot{p}, & p \geqslant b, \\ 0, & -b < p < b, \\ c_2 \dot{p}, & p \leqslant -b. \end{cases} \tag{4c}$$

In the above equation, $m_e = 1/(\lambda_p^2/I_p + \lambda_g^2/I_g)$, mesh damping is assumed to be

$$\zeta = \frac{q k_{1m}}{2 m_{em} \omega_n} = \frac{q \omega_n}{2}, \tag{5}$$

$$c_i = q k_i = \frac{2\zeta}{\omega_n} k_i, \quad i = 1, 2, \tag{6}$$

where $\omega_n = \sqrt{k_{1m}/m_{em}}$, $m_{em} = 1/(\lambda_{pm}^2/I_p + \lambda_{gm}^2/I_g)$. The time-varying mesh parameters can be expressed as a Fourier series given by

$$\lambda_p = \lambda_{pm} + \sum_{j=1}^{\infty} \lambda_{paj} \cos(j\omega t + \phi_{pj}), \tag{7}$$

$$\lambda_g = \lambda_{gm} + \sum_{j=1}^{\infty} \lambda_{gaj} \cos(j\omega t + \phi_{gj}), \tag{8}$$

$$e = \sum_{j=1}^{\infty} e_{aj} \cos(j\omega t + \phi_{ej}), \tag{9}$$

$$k_1 = k_{1m} + \sum_{j=1}^{\infty} k_{1aj} \cos(j\omega t + \phi_{k1j}), \tag{10}$$

$$k_2 = k_{2m} + \sum_{j=1}^{\infty} k_{2aj} \cos(j\omega t + \phi_{k2j}). \tag{11}$$

In the fundamental harmonic form, they can be described as

$$\lambda_p = \lambda_{pm} + \lambda_{pa1}\cos(\omega t + \phi_{p1}), \tag{12}$$

$$\lambda_g = \lambda_{gm} + \sum_{j=1}^{\infty} \lambda_{gaj}\cos(j\omega t + \phi_{gj}), \tag{13}$$

$$e = e_{a1}\cos(\omega t + \phi_{e1}), \tag{14}$$

$$k_1 = k_{1m} + k_{1a1}\cos(\omega t + \phi_{k11}), \tag{15}$$

$$k_2 = k_{2m} + k_{2a1}\cos(\omega t + \phi_{k21}). \tag{16}$$

Dynamic mesh force can be computed from

$$F_m = g(\dot{p}) + f(p). \tag{17}$$

For simplicity, a dimensionless form of Eq. (4a) can be obtained by assuming the following equalities:

$$\tilde{p} = \frac{p}{b}, \tag{18}$$

$$\tilde{t} = \omega_n t, \tag{19}$$

$$\tilde{\omega} = \frac{\omega}{\omega_n}, \tag{20}$$

$$\tilde{\lambda}_p = \frac{\lambda_p}{\lambda_{pm}}, \tag{21}$$

$$\tilde{\lambda}_g = \frac{\lambda_g}{\lambda_{gm}}, \tag{22}$$

$$\tilde{k}_1 = \frac{k_1}{k_{1m}}, \tag{23}$$

$$\tilde{k}_2 = \frac{k_2}{k_{2m}}, \tag{24}$$

$$\tilde{e} = \frac{e}{b}. \tag{25}$$

Applying the above expressions, the dimensionless mesh parameters can then be expressed as

$$\tilde{\lambda}_p = 1 + \tilde{\lambda}_{pa1}\cos(\tilde{\omega}\tilde{t} + \phi_{p1}), \tag{26}$$

$$\tilde{\lambda}_g = 1 + \tilde{\lambda}_{ga1}\cos(\tilde{\omega}\tilde{t} + \phi_{g1}), \tag{27}$$

$$\tilde{k}_1 = 1 + \tilde{k}_{1a1}\cos(\tilde{\omega}\tilde{t} + \phi_{k11}), \tag{28}$$

$$\tilde{k}_2 = 1 + \tilde{k}_{2a1}\cos(\tilde{\omega}\tilde{t} + \phi_{k21}), \tag{29}$$

$$\tilde{e} = \tilde{e}_{a1}\cos(\tilde{\omega}\tilde{t} + \phi_{e1}). \tag{30}$$

Subsequently, the dimensionless form of Eq. (4a) can be obtained as

$$\tilde{p}'' + 2\zeta\frac{(\tilde{\lambda}_p^2 + \eta\tilde{\lambda}_g^2)}{(1+\eta)}\tilde{g}(\tilde{p}') + \frac{(\tilde{\lambda}_p^2 + \eta\tilde{\lambda}_g^2)}{(1+\eta)}\tilde{f}(\tilde{p}) = \tilde{\lambda}_p\tilde{T}_p + \tilde{\lambda}_g\tilde{T}_g - \tilde{e}'', \tag{31a}$$

$$\tilde{f}(\tilde{p}) = \begin{cases} \tilde{k}_1(\tilde{p}-1), & \tilde{p} \geqslant 1, \\ 0, & -1 < \tilde{p} < 1, \\ r_k\tilde{k}_2(\tilde{p}+1), & \tilde{p} \leqslant -1, \end{cases} \tag{31b}$$

$$\tilde{g}(\tilde{p}') = \begin{cases} \tilde{k}_1\tilde{p}', & \tilde{p} \geqslant 1, \\ 0, & -1 < \tilde{p} < 1, \\ r_k\tilde{k}_2\tilde{p}', & \tilde{p} \leqslant -1, \end{cases} \tag{31c}$$

where some of the symbols used above can be expressed as

$$\tilde{T}_p = \frac{\lambda_{pm} T_p}{b\omega_n^2 I_p}, \tag{32}$$

$$\tilde{T}g = \eta \tilde{T}_p, \tag{33}$$

$$\eta = \frac{\lambda_{gm}^2 I_p}{\lambda_{pm}^2 I_g}. \tag{34}$$

The mean mesh stiffness ratio r_k is described as

$$r_k = \frac{k_{2m}}{k_{1m}}. \tag{35}$$

The dimensionless dynamic mesh force can be calculated as

$$\tilde{F}_m = 2\zeta\tilde{g}(\tilde{p}') + \tilde{f}(\tilde{p}). \tag{36}$$

At this point, it is necessary to define the various tooth impact conditions that will be discussed in the subsequent parametric studies. If the dynamic response $\tilde{p}$ in Eq. (18) is always greater than positive one, no tooth impact between the driver and driven gear exist since the tooth pair is always in contact. This is described mathematically in the top condition in Eqs. (31b) and (31c). On the other hand, if $\tilde{p}$ does creep into the regime defined by the middle condition in Eqs. (31b) and (31c) where it becomes less than positive one but still greater than negative one during certain period of time, it will give rise to single-sided tooth impact. In this case, the tooth pair that is supposedly in contact momentarily loses contact because the dynamic load exceeds the drive torque. Finally, if $\tilde{p}$ does vary substantially to the point that it also moves into the regime of less than negative one during part of the time as shown by the last condition in Eqs. (31b) and (31c), this will produce a double-sided tooth impact case where the driver tooth collides with both the forward and backward driven teeth. It will be shown later that when tooth impact occurs, the dynamic response will produce jumps in the response and other behaviors that are characteristics of highly nonlinear systems.

Proceeding on to derive the final form of the dimensionless model, Eqs. (26)–(30) can be substituted into Eq. (31a) to yield a nonlinear time-varying equation of motion in the form of

$$\begin{aligned} \tilde{p}'' + 2\zeta & \frac{((1+\tilde{\lambda}_{pa1}\cos(\tilde{\omega}\tilde{t}+\phi_{p1}))^2 + \eta(1+\tilde{\lambda}_{ga1}\cos(\tilde{\omega}\tilde{t}+\phi_{g1}))^2)}{(1+\eta)}\tilde{g}(\tilde{p}') \\ & + \frac{((1+\tilde{\lambda}_{pa1}\cos(\tilde{\omega}\tilde{t}+\phi_{p1}))^2 + \eta(1+\tilde{\lambda}_{ga1}\cos(\tilde{\omega}\tilde{t}+\phi_{g1}))^2)}{(1+\eta)}\tilde{f}(\tilde{p}) \\ & = (1+\tilde{\lambda}_{pa1}\cos(\tilde{\omega}\tilde{t}+\phi_{p1}) + \eta(1+\tilde{\lambda}_{ga1}\cos(\tilde{\omega}\tilde{t}+\phi_{g1})))\tilde{T}_p \\ & \quad + \tilde{\omega}^2\tilde{e}_{a1}\cos(\tilde{\omega}\tilde{t}+\phi_{e1}). \end{aligned} \tag{37}$$

Since there is no analytical method presently available to treat this highly nonlinear equation (37), it is solved by numerical means here. In this study, the explicit Runge–Kutta integration routine with variable step is applied because of its known capability to handle strong nonlinearity. Applying this numerical integration routine, the dynamic response $\tilde{p}$ is obtained. From the standard deviation value and mean value of $\tilde{p}$ at each

frequency point $\tilde{\omega}$, the variational and mean dynamic responses are calculated. The dynamic mesh force is then computed according to Eq. (36). The algorithm is implemented in MATLAB [10] that is a widely used general-purpose matrix and numerical calculation program.

3. Computational results

A typical automotive-size hypoid gear pair is used as the numerical example. Applying a quasi-static tooth contact analysis [8] that generates a large quantity of highly detailed load and pattern distributions, the reduced order mesh parameters used in the construction of the lumped parameter model are obtained [8] as described in the previous section. The mesh stiffness inherently includes the contact nonlinearity effect since it is obtained by post-processing the output data from a tooth contact analysis that explicitly formulates the nonlinear contact problem. The corresponding dimensionless values along with other system parameters for the baseline gear design are shown in Table 1. Subsequent parametric studies consider the deviation of mesh parameters from this initial set of values.

Applying the nonlinear time-varying dynamic model described by Eq. (37), the effects of asymmetric mesh stiffness parameters, such as mean mesh stiffness ratio r_k, mesh stiffness variations $\tilde{k}_{1a1}$ and $\tilde{k}_{2a1}$, mesh stiffness phase angles ϕ_{k11} and ϕ_{k21}, on the dynamic mesh force response and tooth impact regions are examined next.

3.1. Effect of mean mesh stiffness ratio r_k

The effect of mean mesh stiffness ratio r_k on dynamic response for both light and heavy loads is shown in Figs. 2 and 4, respectively. For light load at $r_k = 0.25$, a softening response jump occurs at the primary resonance. When r_k is increased to 0.5, besides a softening response jump, a hardening response jump also appears at a higher frequency. As r_k is increased further to the value of 2, the multi-valued region between response jump up and down transition frequencies increases. Also, as r_k is increased, the dynamic mesh force amplitude increases. It is noted that only double-sided tooth impact region is affected considerably by r_k, while single-sided tooth impact and no impact regions are nearly unchanged. To explain the phenomena, the accompanying time-history plots are used as shown in Fig. 3. In Fig. 3(b)–(d), no impact, single-sided tooth impact and double-sided tooth impact response are shown, respectively. For no impact response $\tilde{p} \in (1, +\infty)$, for single-sided impact $\tilde{p} \in (-1, +\infty)$ and for double-sided impact $\tilde{p} \in (-\infty, +\infty)$ as described earlier. According to Eqs. (31b) and (31c), r_k takes effect only in the case of double-sided tooth impact. It does not come into play for no impact and single-sided tooth impact. For heavy load, the effect of r_k on the dynamic response is almost negligible. So, an increase of r_k tends to worsen hypoid gear dynamics primarily for lightly loaded condition (Fig. 4).

Table 1
Dimensionless dynamic parameters for a typical automotive hypoid gear pair

Parameter symbols	Numerical values
$\tilde{T}_p$	2.01
ξ	0.05
η	0.74
r_k	1.24
$\tilde{\lambda}_{pa1}, \tilde{\lambda}_{ga1}$	0.01
ϕ_{p1}, ϕ_{g1}	0.22π
$\tilde{e}_{a1}$	0.49
ϕ_{e1}	0.74π
$\tilde{k}_{1a}$	0.05
$\tilde{k}_{2a}$	0.05
ϕ_{k1}	-0.57π
ϕ_{k2}	-0.75π

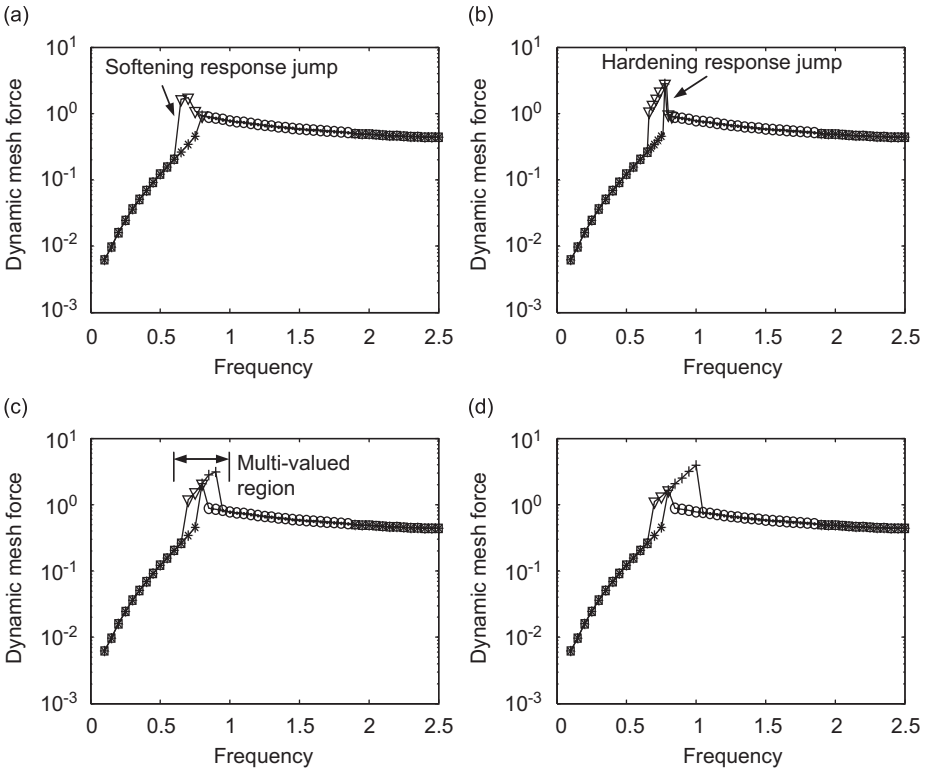

Fig. 2. Dimensionless dynamic mesh force $\tilde{F}_m$ versus dimensionless frequency $\tilde{\omega}$ for different mean mesh stiffness ratios for lightly loaded case. $\tilde{T}_p = 0.4$, (a) $r_k = 0.25$, (b) $r_k = 0.5$, (c) $r_k = 1$, (d) $r_k = 2$. ✳, □—no impact; ·, ○—single-sided impact; +, ▽—double-sided impact; ———, ✳, ·, +—increasing frequency; - - - -, □, ○,▽—decreasing frequency.

3.2. Effect of mesh stiffness variations $\tilde{k}_{1a1}$ and $\tilde{k}_{2a1}$

Normally, $\tilde{k}_{1a1}$ is close to $\tilde{k}_{2a1}$ according to the calculation results, and hence it is reasonable to assume $\tilde{k}_{1a1} = \tilde{k}_{2a1}$ first. The cases for $\tilde{k}_{1a1} \neq \tilde{k}_{2a1}$ are discussed later. When $\tilde{k}_{1a1} = \tilde{k}_{2a1}$, the effects of $\tilde{k}_{1a1}$ and $\tilde{k}_{2a1}$ for light load case is shown in Fig. 5. For the current light load case, we observed that as $\tilde{k}_{1a1}$ and $\tilde{k}_{2a1}$ are increased from 0 to 0.1, the dynamic mesh force response does not change much. As $\tilde{k}_{1a1}$ and $\tilde{k}_{2a1}$ are increased to 0.2, it can be observed that more response jump discontinuities and double-sided tooth impacts appear at higher frequencies, a parametric resonance occurs at $\tilde{\omega} = 0.5$, and dynamic mesh force amplitude increases.

When $\tilde{k}_{1a1} = \tilde{k}_{2a1}$, the effects of $\tilde{k}_{1a1}$ and $\tilde{k}_{2a1}$ for heavy load are shown in Fig. 6. For $\tilde{k}_{1a1} = \tilde{k}_{2a1} = 0$, there is a small softening response jump and no double-sided tooth impact can be seen. As $\tilde{k}_{1a1}$ and $\tilde{k}_{2a1}$ are increased to 0.05, a larger response jump and double-sided tooth impacts occur at the primary resonance frequency. For $\tilde{k}_{1a1} = \tilde{k}_{2a1} = 0.1$, besides a softening response jump and a hardening response jump occurring in the vicinity of the resonance frequency, a parametric resonance occurs at $\tilde{\omega} = 0.5$. For $\tilde{k}_{1a1} = \tilde{k}_{2a1} = 0.2$, a softening response jump and a hardening response jump can be observed at the resonance frequency, the region between response jump up and down frequencies increases, and parametric resonance is more evident at $\tilde{\omega} = 0.5$. Hence, as $\tilde{k}_{1a1}$ and $\tilde{k}_{2a1}$ are increased, the dynamic mesh force amplitude increases considerably. From these observations, we can conclude that an increase of $\tilde{k}_{1a1}$ and $\tilde{k}_{2a1}$ will worsen the dynamics especially for heavy load case.

Although $\tilde{k}_{1a1}$ and $\tilde{k}_{2a1}$ are normally close to each other, they may be different in some special cases. When $\tilde{k}_{1a1} \neq \tilde{k}_{2a1}$, the effect of different mesh stiffness variations for light load is shown in Fig. 7. For $\tilde{k}_{1a1} = 0.05$, both response jump phenomenon and tooth impacts can be observed clearly. As $\tilde{k}_{1a1}$ is increased to 0.1, the response does not show much change. As $\tilde{k}_{1a1}$ is increased further to 0.2, the response jump region at the

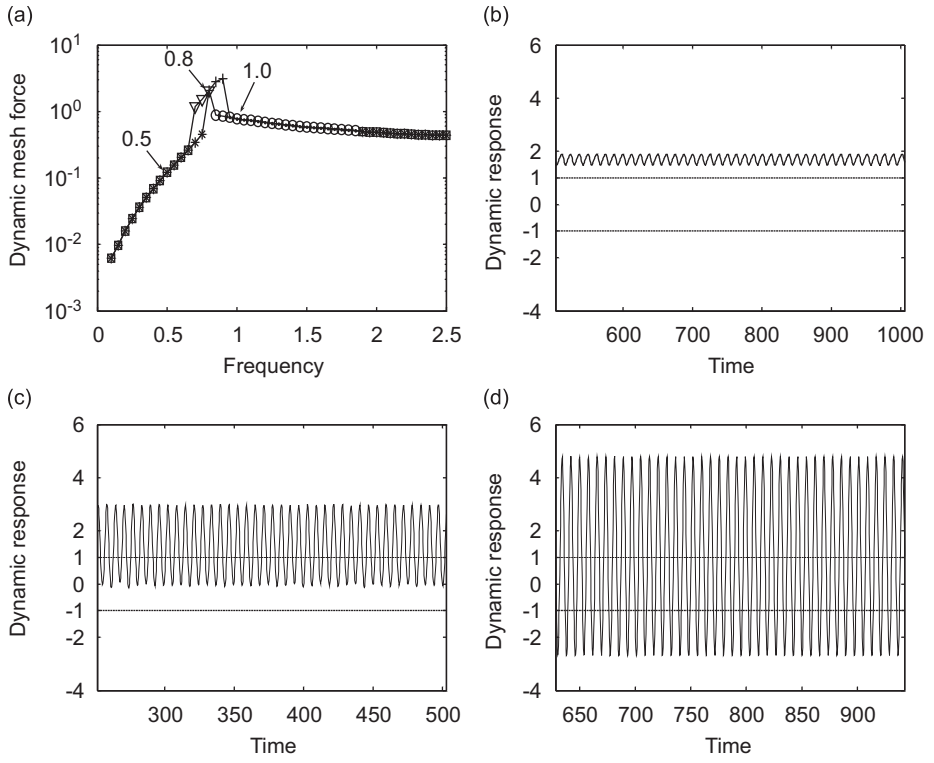

Fig. 3. Dimensionless dynamic responses for $r_k = 1$ for lightly loaded case: (a) dimensionless dynamic mesh force $\tilde{F}_m$, (b) dimensionless dynamic response $\tilde{p}$ at $\tilde{\omega} = 0.5$ with no tooth impact, (c) dimensionless dynamic response $\tilde{p}$ at $\tilde{\omega} = 1.0$ with single-sided tooth impact, (d) dimensionless dynamic response $\tilde{p}$ at $\tilde{\omega} = 0.8$ with double-sided tooth impact. ⁎, □—no impact; ·, ○—single-sided impact; +, ▽—double-sided impact; ———, ⁎, ·, +—increasing frequency; - - - -, □, ○,▽—decreasing frequency.

resonance increases, more response jumps and double-sided impacts occur at higher frequencies, and parametric resonance can be seen at $\tilde{\omega} = 0.5$. Also, as $\tilde{k}_{1a1}$ is increased from 0.05 to 0.2, the amplitude of dynamic mesh force increases. On the other hand, as $\tilde{k}_{2a1}$ is increased from 0.05 to 0.2, the response portrays almost no change. This shows that $\tilde{k}_{1a1}$ affects dynamic response more than $\tilde{k}_{2a1}$.

When $\tilde{k}_{1a1} \neq \tilde{k}_{2a1}$, the effect of different mesh stiffness variations for heavily loaded case is shown in Fig. 8. At $\tilde{k}_{1a1} = 0.05$, a softening response jump and tooth impacts appear in Fig. 8(a). As $\tilde{k}_{1a1}$ is increased to 0.1 in Fig. 8(b), besides a softening response jump and a hardening response jump occurring at the resonance, parametric resonance also occurs at $\tilde{\omega} = 0.5$. At $\tilde{k}_{1a1} = 0.2$ as plotted in Fig. 8(c), more significant response jumps with wider frequency region can be seen at the resonance, and the parametric resonance at $\tilde{\omega} = 0.5$ can be observed more clearly. As $\tilde{k}_{1a1}$ is increased from 0.05 to 0.2 leaving $\tilde{k}_{2a1}$ unchanged, the dynamic mesh force increases significantly. On the other hand, when $\tilde{k}_{2a1}$ is increased from 0.05 to 0.2 while maintaining $\tilde{k}_{1a1}$ the same as the baseline design, the dynamic mesh force remains almost unchanged. This result again shows that $\tilde{k}_{1a1}$ affects dynamic response more than $\tilde{k}_{2a1}$, especially for heavily loaded case.

3.3. Effect of mesh stiffness phase angles ϕ_{k11} and ϕ_{k21}

According to Eqs. (28) and (29), when $\tilde{k}_{1a1}$ and $\tilde{k}_{2a1}$ are equal to zero, ϕ_{k11} and ϕ_{k21} have no effect on the dynamic response at all. Similarly, when $\tilde{k}_{1a1}$ and $\tilde{k}_{2a1}$ are very small (less than 0.05), the numerical results indicate that ϕ_{k11} and ϕ_{k21} have little effect on the dynamic response. For brevity, these results are not shown here. However when $\tilde{k}_{1a1}$ and $\tilde{k}_{2a1}$ are increased further to 0.2, the predicted results in Figs. 9 and 10 for light and heavy load conditions, respectively, show that both ϕ_{k11} and ϕ_{k21} do have a noticeable effect on the gear dynamic response. The light load operating condition will be discussed first.

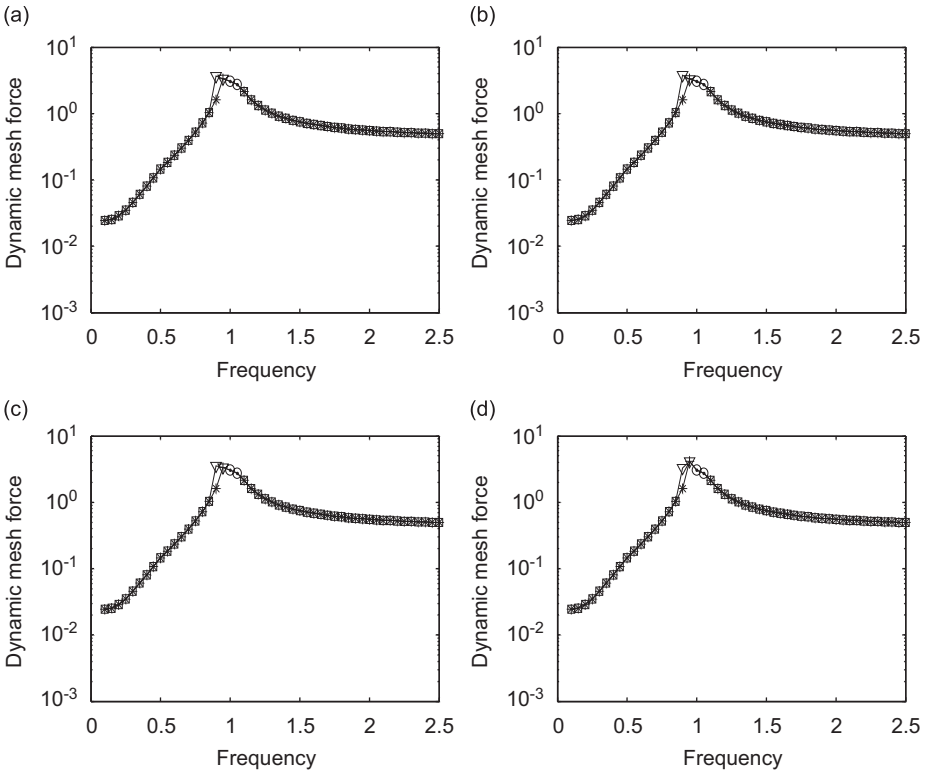

Fig. 4. Dimensionless dynamic mesh force $\tilde{F}_m$ versus dimensionless frequency $\tilde{\omega}$ for different mean mesh stiffness ratios for heavily loaded case. $\tilde{T}_p = 2.01$, (a) $r_k = 0.25$, (b) $r_k = 0.5$, (c) $r_k = 1$, (d) $r_k = 2$. ✳, □—no impact; ·, ○—single-sided impact; +, ▽—double-sided impact; ———, ✳, ·, +—increasing frequency; ----, □, ○,▽—decreasing frequency.

At the assumed baseline values of $\phi_{k11} = 0.57\pi$ and $\phi_{k21} = 0.75\pi$ as shown in Fig. 9(a) for lightly loaded gears, both response jump discontinuities and tooth impacts can be clearly observed, as expected, based on results presented in the earlier part of this paper. As ϕ_{k11} is increased to 0.07π while keeping ϕ_{k21} the same as illustrated in Fig. 9(b), the response jumps become a little more prevalent at resonance and higher frequencies. On the other hand, for $\phi_{k11} = 0.43\pi$ in Fig. 9(c), the response jump region at resonance becomes narrower, no response jump is seen at higher frequencies and the overall amplitude decreases considerably. As ϕ_{k11} is increased further to 0.93π in Fig. 9(d), the response jump diminishes some more. In contrast, as ϕ_{k21} is increased from 0.75π to 0.25π while fixing $\phi_{k11} = 0.57\pi$ in Fig. 9(e), the response does not portrays any significant change from the baseline response in Fig. 9(a). As ϕ_{k21} is increased further to 0.25π in Fig. 9(f), the response amplitude increases. For $\phi_{k21} = 0.75\pi$ in Fig. 9(g), the jump region at resonance becomes wider and the amplitude also increases some more. This shows that only double-sided tooth impact response is affected by ϕ_{k21}, while single-sided tooth impact and no impact response are essentially unaffected. The reason is because, according to Eqs. (31b) and (31c), ϕ_{k21} only takes effect for double-sided tooth impact condition. Furthermore, the change in ϕ_{k11} affects the hypoid gear dynamic response more than the change in ϕ_{k21}.

The effects of ϕ_{k11} and ϕ_{k21} for heavily loaded case when $\tilde{k}_{1a1} = \tilde{k}_{2a1} = 0.2$ is discussed next. Fig. 10(a) shows the dynamic response for the assumed baseline values of $\phi_{k11} = 0.57\pi$ and $\phi_{k21} = 0.75\pi$. As expected, less response jump discontinuities and tooth impacts exist compared to lightly loaded case result in Fig. 9(a). As ϕ_{k11} is increased to 0.07π without changing ϕ_{k21} in Fig. 10(b), the response jumps at resonance becomes larger. At $\phi_{k11} = 0.43\pi$ in Fig. 10(c), only a softening response jump and less tooth impacts appear at the resonance, and the response amplitude drops considerably. As ϕ_{k11} is increased further to 0.93π in Fig. 10(d), no response jump can be observed at all and only single-sided tooth impact occurs at the resonance. As ϕ_{k21} is increased from 0.75π to 0.75π while keeping ϕ_{k11} the same in Fig. 10(e–g), the response does not show much change from Fig. 10(a) except that the response jumps become a little larger and the response amplitude

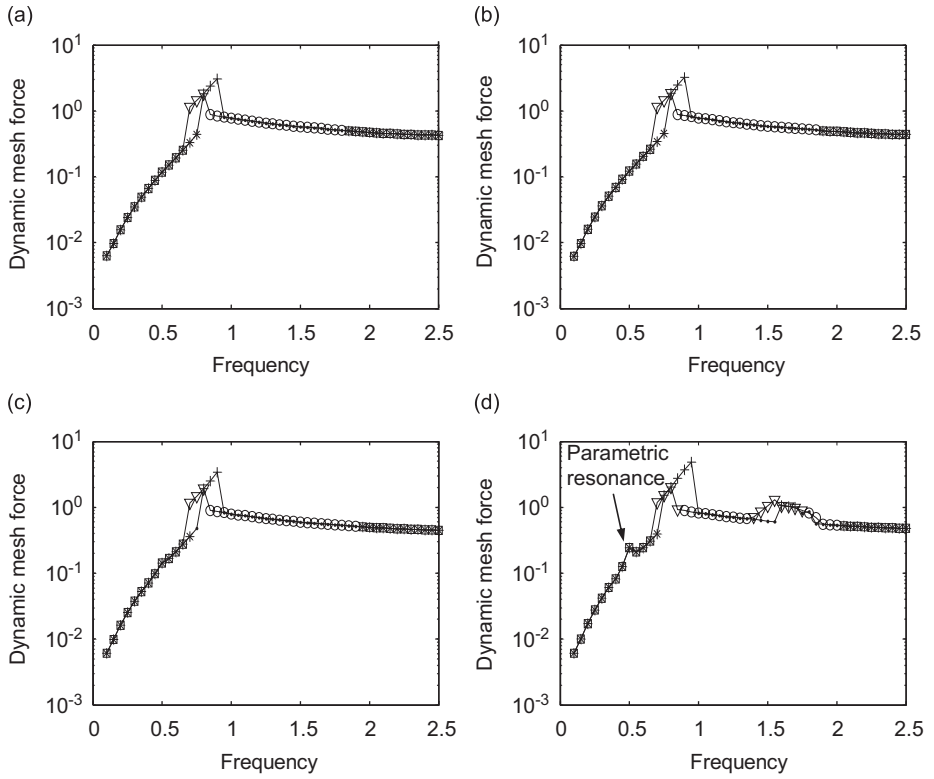

Fig. 5. Dimensionless dynamic mesh force $\tilde{F}_m$ versus dimensionless frequency $\tilde{\omega}$ for different mesh stiffness variation values for lightly loaded case. $\tilde{T}_p = 0.4$, (a) $\tilde{k}_{1a1} = \tilde{k}_{2a1} = 0$, (b) $\tilde{k}_{1a1} = \tilde{k}_{2a1} = 0.05$, (c) $\tilde{k}_{1a1} = \tilde{k}_{2a1} = 0.1$, (d) $\tilde{k}_{1a1} = \tilde{k}_{2a1} = 0.2$. $\ast$, □—no impact; $\cdot$, ○ single-sided impact; +, ▽—double-sided impact; ———, $\ast$, $\cdot$, +—increasing frequency; - - - -, □, ○,▽—decreasing frequency.

increases. Similar to the light load condition, only double-sided tooth impact region is affected by ϕ_{k21}, while single-sided tooth impact and no impact regions remain about the same. Also, change in ϕ_{k11} affects the dynamic response more than variation in ϕ_{k21}.

4. Dynamic models with different nonlinearities

Two types of nonlinearities exist in Eq. (31a): one is the mesh stiffness asymmetry, and the other is backlash. In this section, we will examine the separate and combined effects of these two nonlinear characteristics using dynamic models possessing different types of nonlinearities.

If the nonlinearity in the hypoid gear pair model comprises of only mesh stiffness asymmetry and no backlash, Eq. (31a) can be reduced to

$$\tilde{p}'' + 2\zeta\frac{(\tilde{\lambda}_p^2 + \eta\tilde{\lambda}_g^2)}{(1+\eta)}\tilde{g}_1(\tilde{p}') + \frac{(\tilde{\lambda}_p^2 + \eta\tilde{\lambda}_g^2)}{(1+\eta)}\tilde{f}_1(\tilde{p}) = (\tilde{\lambda}_p + \eta\tilde{\lambda}_g)\tilde{T}_p - \tilde{e}'', \tag{38a}$$

$$\tilde{f}_1(\tilde{p}) = \begin{cases} \tilde{k}_1\tilde{p}, & \tilde{p} \geqslant 0, \\ r_k\tilde{k}_2\tilde{p}, & \tilde{p} < 0, \end{cases} \tag{38b}$$

$$\tilde{g}_1(\tilde{p}') = \begin{cases} \tilde{k}_1\tilde{p}', & \tilde{p} \geqslant 0, \\ r_k\tilde{k}_2\tilde{p}', & \tilde{p} < 0. \end{cases} \tag{38c}$$

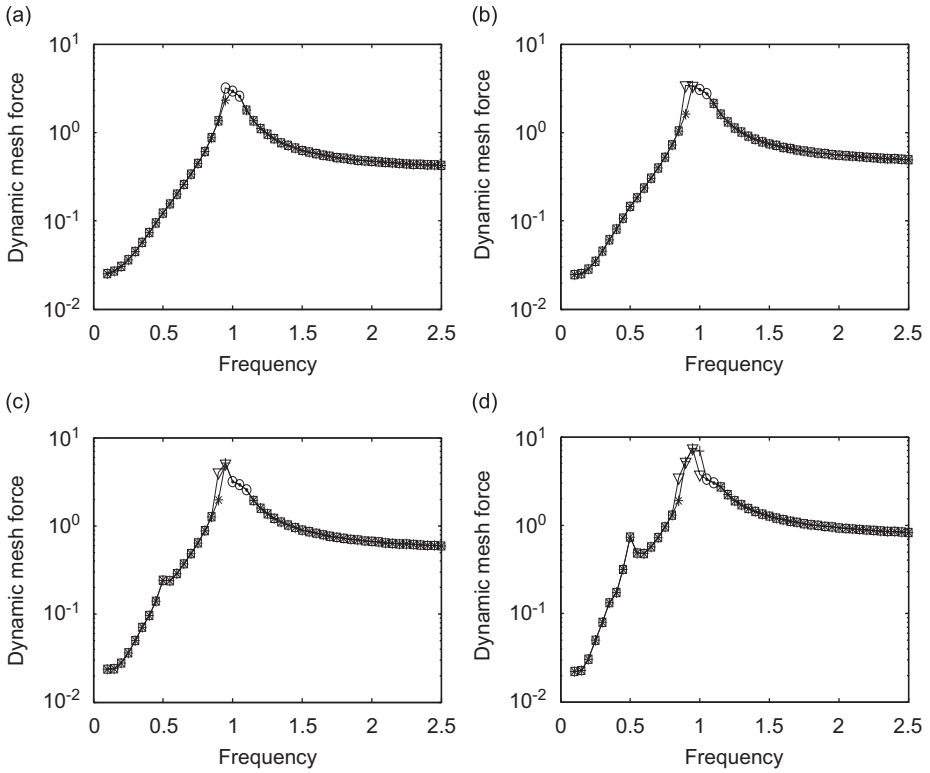

Fig. 6. Dimensionless dynamic mesh force $\tilde{F}_m$ versus dimensionless frequency $\tilde{\omega}$ for different mesh stiffness variation values for heavily loaded case. $\tilde{T}_p = 2.01$, (a) $\tilde{k}_{1a1} = \tilde{k}_{2a1} = 0$, (b) $\tilde{k}_{1a1} = \tilde{k}_{2a1} = 0.05$, (c) $\tilde{k}_{1a1} = \tilde{k}_{2a1} = 0.1$, (d) $\tilde{k}_{1a1} = \tilde{k}_{2a1} = 0.2$. ∗, □—no impact; ·, ○—single-sided impact; +, ▽—double-sided impact; ———, ∗, ·, +—increasing frequency; ----, □, ○,▽—decreasing frequency.

Assuming $\tilde{k}_1 = \tilde{k}_2 = \tilde{k}$, then Eq. (38a) can be further reduced to

$$\tilde{p}'' + 2\zeta\frac{(\tilde{\lambda}_p^2 + \eta\tilde{\lambda}_g^2)}{(1+\eta)}\tilde{k}\tilde{g}_2(\tilde{p}') + \frac{(\tilde{\lambda}_p^2 + \eta\tilde{\lambda}_g^2)}{(1+\eta)}\tilde{k}\tilde{f}_2(\tilde{p}) = (\tilde{\lambda}_p + \eta\tilde{\lambda}_g)\tilde{T}_p - \tilde{e}'', \tag{39a}$$

$$\tilde{f}_2(\tilde{p}) = \begin{cases} \tilde{p}, & \tilde{p} \geqslant 0, \\ r_k\tilde{p}, & \tilde{p} < 0, \end{cases} \tag{39b}$$

$$\tilde{g}_2(\tilde{p}') = \begin{cases} \tilde{p}', & \tilde{p} \geqslant 0, \\ r_k\tilde{p}', & \tilde{p} < 0, \end{cases} \tag{39c}$$

where the nonlinear displacement function $\tilde{f}_2(\tilde{p})$ is shown in Fig. 11(a).

Alternatively, if the nonlinearity comprises of only backlash with symmetric mesh stiffness, i.e. $\tilde{k}_1 = \tilde{k}_2 = \tilde{k}$ and $r_k = 1$, Eq. (31a) can be simplified as

$$\tilde{p}'' + 2\zeta\frac{(\tilde{\lambda}_p^2 + \eta\tilde{\lambda}_g^2)}{(1+\eta)}\tilde{k}\tilde{g}_3(\tilde{p}') + \frac{(\tilde{\lambda}_p^2 + \eta\tilde{\lambda}_g^2)}{(1+\eta)}\tilde{k}\tilde{f}_3(\tilde{p}) = (\tilde{\lambda}_p + \eta\tilde{\lambda}_g)\tilde{T}_p - \tilde{e}'', \tag{40a}$$

$$\tilde{f}_3(\tilde{p}) = \begin{cases} (\tilde{p}-1), & \tilde{p} \geqslant 1, \\ 0, & -1 < \tilde{p} < 1, \\ (\tilde{p}+1), & \tilde{p} \leqslant -1, \end{cases} \tag{40b}$$

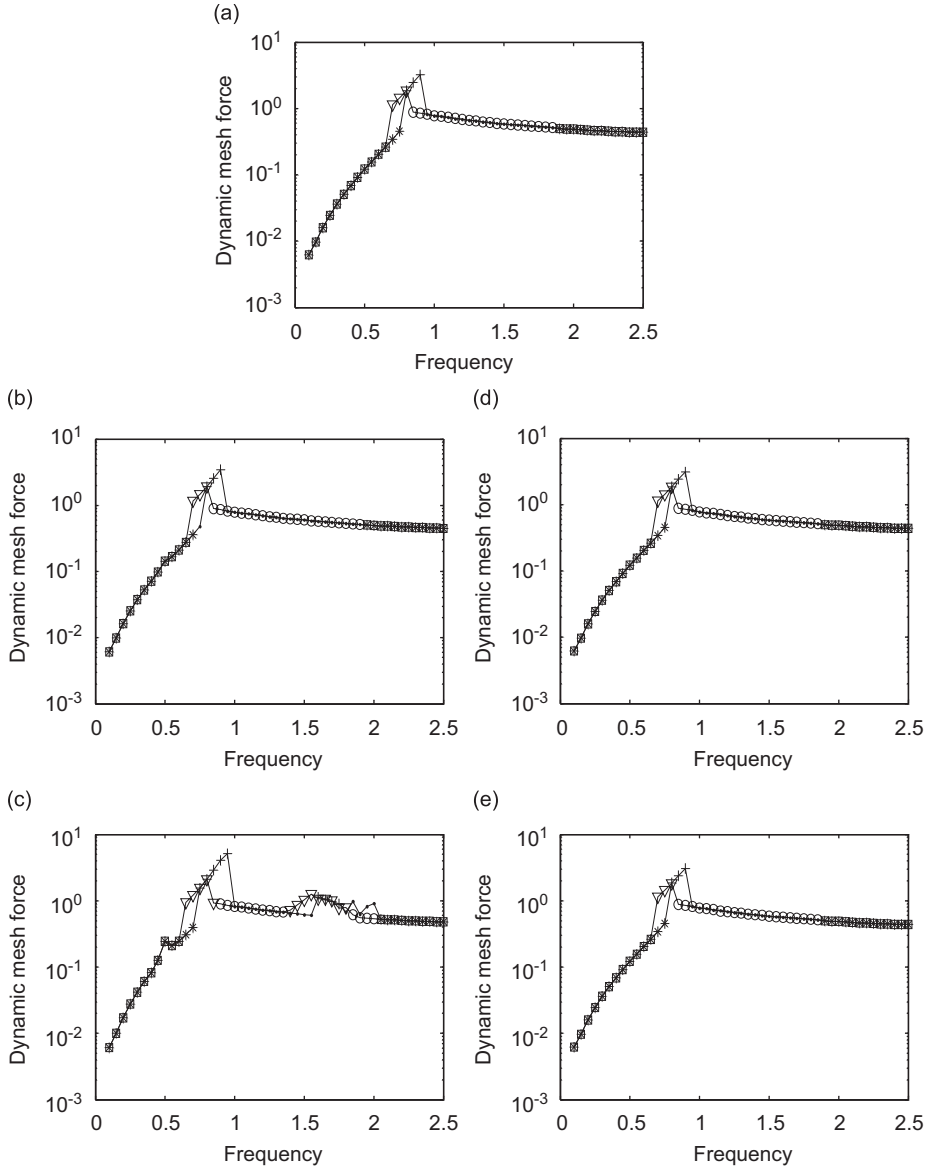

Fig. 7. Dimensionless dynamic mesh force $\tilde{F}_m$ versus dimensionless frequency $\tilde{\omega}$ for different mesh stiffness variations for lightly loaded case. $\tilde{T}_p = 0.4$, (a) $\tilde{k}_{1a1} = \tilde{k}_{2a1} = 0.05$, (b) $\tilde{k}_{1a1} = 0.1$, $\tilde{k}_{2a1} = 0.05$, (c) $\tilde{k}_{1a1} = 0.2$, $\tilde{k}_{2a1} = 0.05$, (d) $\tilde{k}_{1a1} = 0.05$, $\tilde{k}_{2a1} = 0.1$, (e) $\tilde{k}_{1a1} = 0.05$, $\tilde{k}_{2a1} = 0.2$. ⁎, □—no impact; ·, ○—single-sided impact; +, ▽—double-sided impact; ———, ⁎, ·, +—increasing frequency; - - - -, □, ○,▽—decreasing frequency.

$$\tilde{g}_3(\tilde{p}') = \begin{cases} \tilde{p}', & \tilde{p} \geqslant 1, \\ 0, & -1 < \tilde{p} < 1, \\ \tilde{p}', & \tilde{p} \leqslant -1, \end{cases} \tag{40c}$$

where the nonlinear displacement function $\tilde{f}_3(\tilde{p})$ is shown in Fig. 11(b). The above equations (40a)–(40c) can be partially validated by its special case for spur gear. For spur gear, where $\tilde{\lambda}_p = \tilde{\lambda}_g = 1$, Eq. (40a) can be further reduced to

$$\tilde{p}'' + 2\zeta\tilde{k}\tilde{g}_3(\tilde{p}') + \tilde{k}\tilde{f}_3(\tilde{p}) = (1+\eta)\tilde{T}_p - \tilde{e}'', \tag{41}$$

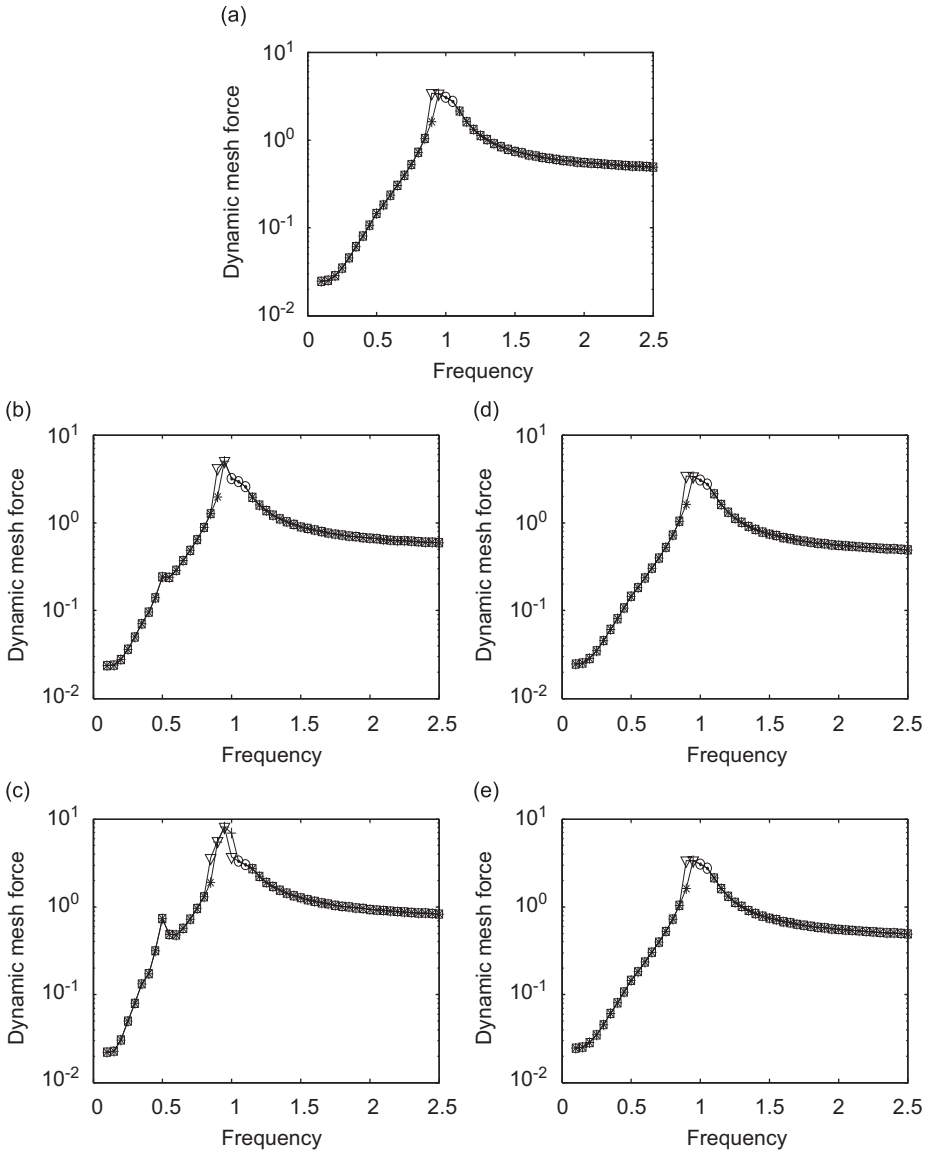

Fig. 8. Dimensionless dynamic mesh force $\tilde{F}_m$ versus dimensionless frequency $\tilde{\omega}$ for different mesh stiffness variations for heavily loaded case. $\tilde{T}_p = 2.01$, (a) $\tilde{k}_{1a1} = \tilde{k}_{2a1} = 0.05$, (b) $\tilde{k}_{1a1} = 0.1$, $\tilde{k}_{2a1} = 0.05$, (c) $\tilde{k}_{1a1} = 0.2$, $\tilde{k}_{2a1} = 0.05$, (d) $\tilde{k}_{1a1} = 0.05$, $\tilde{k}_{2a1} = 0.1$, (e) $\tilde{k}_{1a1} = 0.05$, $\tilde{k}_{2a1} = 0.2$. ⁎, □—no impact; ·, ○—single-sided impact; +, ▽—double-sided impact; ———, ⁎, ·, +—increasing frequency; ----, □, ○,▽—decreasing frequency.

which was previously validated by the benchmark experimental results reported in Ref. [4]. The only difference is that in Ref. [4], a dissimilar damping was used.

Finally, if both mesh stiffness asymmetry and backlash nonlinearities exist, when $\tilde{k}_1 = \tilde{k}_2 = \tilde{k}$ and $r_k \neq 4$, Eq. (31a) reduces to

$$\tilde{p}'' + 2\zeta\frac{(\tilde{\lambda}_p^2 + \eta\tilde{\lambda}_g^2)}{(1+\eta)}\tilde{k}\tilde{g}_4(\tilde{p}') + \frac{(\tilde{\lambda}_p^2 + \eta\tilde{\lambda}_g^2)}{(1+\eta)}\tilde{k}\tilde{f}_4(\tilde{p}) = (\tilde{\lambda}_p + \eta\tilde{\lambda}_g)\tilde{T}_p - \tilde{e}'', \tag{42a}$$

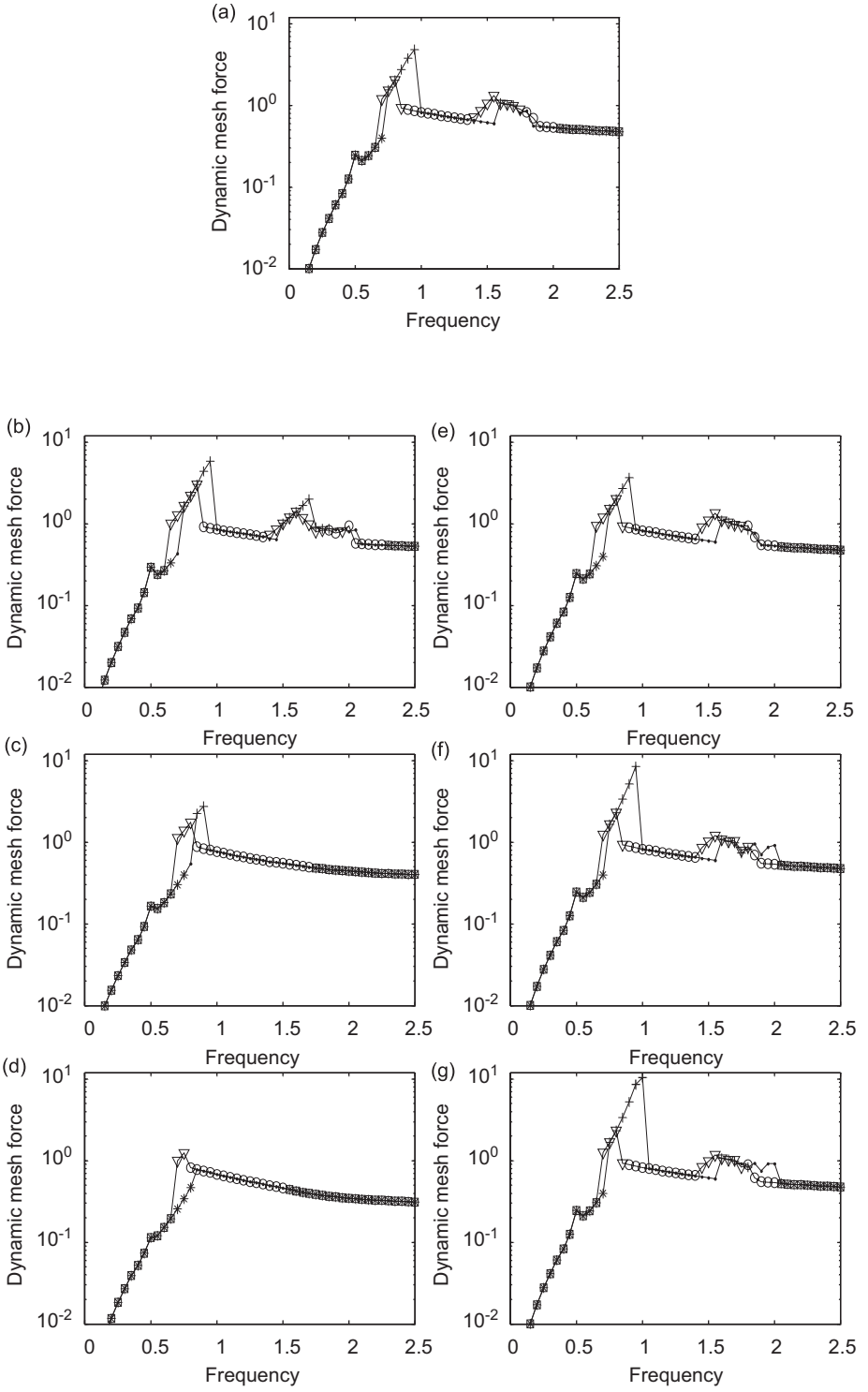

Fig. 9. Dimensionless dynamic mesh force $\tilde{F}_m$ versus dimensionless frequency $\tilde{\omega}$ for different mesh stiffness phase angles for lightly loaded case. $\tilde{T}_p = 0.4$, $\tilde{k}_{1a1} = \tilde{k}_{2a1} = 0.2$, (a) $\phi_{k11} = -0.57\pi$, $\phi_{k21} = -0.75\pi$ (baseline values), (b) $\phi_{k11} = -0.07\pi$, $\phi_{k21} = -0.75\pi$, (c) $\phi_{k11} = 0.43\pi$, $\phi_{k21} = -0.75\pi$, (d) $\phi_{k11} = 0.93\pi$, $\phi_{k21} = -0.75\pi$, (e) $\phi_{k11} = -0.57\pi$, $\phi_{k21} = -0.25\pi$, (f) $\phi_{k11} = -0.57\pi$, $\phi_{k21} = 0.25\pi$, (g) $\phi_{k11} = -0.57\pi$, $\phi_{k21} = 0.75\pi$. $\ast$, □—no impact; ·, ○—single-sided impact; +, ▽—double-sided impact; ———, $\ast$, ·, +—increasing frequency; - - - -, □, ○,▽—decreasing frequency.

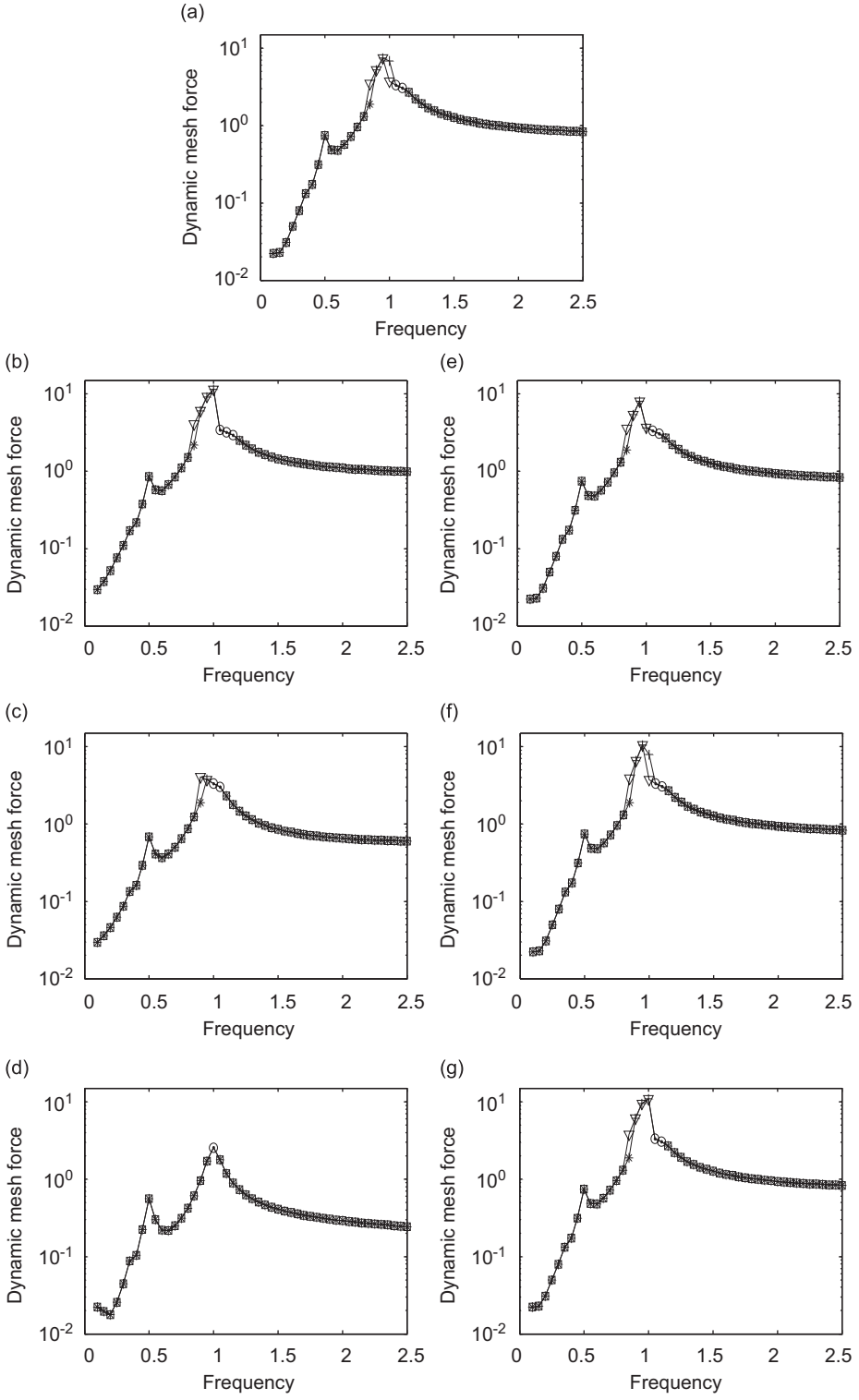

Fig. 10. Dimensionless dynamic mesh force $\tilde{F}_m$ versus dimensionless frequency $\tilde{\omega}$ for different mesh stiffness phase angles for heavily loaded case. $\tilde{T}_p = 2.01$, $\tilde{k}_{1a1} = \tilde{k}_{2a1} = 0.2$, (a) $\phi_{k11} = -0.57\pi$, $\phi_{k21} = -0.75\pi$ (baseline values), (b) $\phi_{k11} = -0.07\pi$, $\phi_{k21} = -0.75\pi$, (c) $\phi_{k11} = 0.43\pi$, $\phi_{k21} = -0.75\pi$, (d) $\phi_{k11} = 0.93\pi$, $\phi_{k21} = -0.75\pi$, (e) $\phi_{k11} = -0.57\pi$, $\phi_{k21} = -0.25\pi$, (f) $\phi_{k11} = -0.57\pi$, $\phi_{k21} = 0.25\pi$, (g) $\phi_{k11} = -0.57\pi$, $\phi_{k21} = 0.75\pi$. $\ast$, □—no impact; ·, ○—single-sided impact; +, ▽—double-sided impact; ———, $\ast$, ·, +—increasing frequency; ----, □, ○, ▽—decreasing frequency.

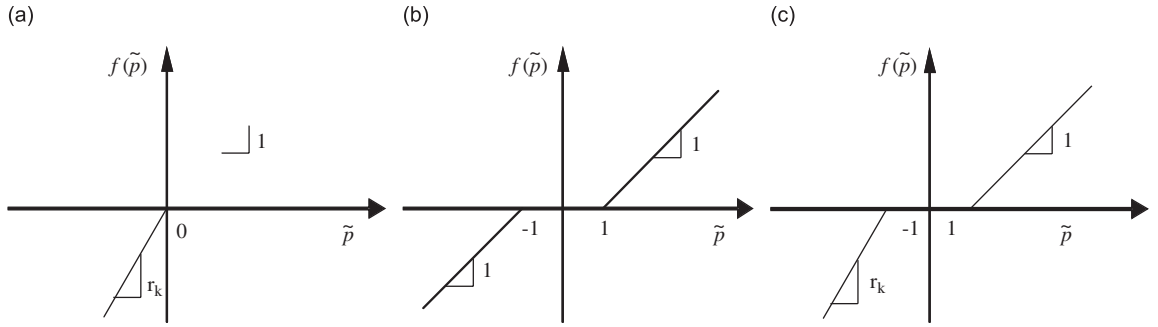

Fig. 11. The nonlinear displacement function: (a) only mesh stiffness asymmetry nonlinearity, (b) only backlash nonlinearity, (c) both mesh stiffness asymmetry and backlash nonlinearities.

$$\tilde{f}_4(\tilde{p}) = \begin{cases} (\tilde{p}-1), & \tilde{p} \geqslant 1, \\ 0, & -1 < \tilde{p} < 1, \\ r_k(\tilde{p}+1), & \tilde{p} \leqslant -1, \end{cases} \tag{42b}$$

$$\tilde{g}_4(\tilde{p}') = \begin{cases} \tilde{p}', & \tilde{p} \geqslant 1, \\ 0, & -1 < \tilde{p} < 1, \\ r_k\tilde{p}', & \tilde{p} \leqslant -1, \end{cases} \tag{42c}$$

where the nonlinear displacement function $\tilde{f}_4(\tilde{p})$ is shown in Fig. 11(c). The corresponding linear time-varying (LTV) equation can be described as

$$\tilde{p}'' + 2\zeta\frac{(\tilde{\lambda}_p^2 + \eta\tilde{\lambda}_g^2)}{(1+\eta)}\tilde{k}\tilde{p}' + \frac{(\tilde{\lambda}_p^2 + \eta\tilde{\lambda}_g^2)}{(1+\eta)}\tilde{k}\tilde{p} = (\tilde{\lambda}_p + \eta\tilde{\lambda}_g)\tilde{T}_p - \tilde{e}''. \tag{43}$$

Next, the effects of mesh stiffness asymmetry nonlinearity, backlash nonlinearity and their interactions are studied numerically for the baseline design using the above three models. Dynamic models with only mesh stiffness asymmetry described by Eqs. (38a)–(38c), with only backlash nonlinearity given by Eqs. (40a)–(40c) and with both types of nonlinearities expressed in Eqs. (31a)–(31c) are compared, and the corresponding dynamic mesh force results for lightly and heavily loaded conditions are shown in Fig. 12(a)–(c) and (d)–(f), respectively. Note that these results have been generated applying the same Runge–Kutta integration routine used earlier.

In Fig. 12(a) that corresponds to light load condition with mesh stiffness asymmetry, the increasing frequency response coincides exactly with the decreasing frequency response. The mesh stiffness asymmetry did not result in any response jump discontinuity, but it did cause a slight shift in the resonance response of the dynamic mesh force compared to the LTV predictions. In Fig. 12(b) that corresponds to light load condition with only backlash, a pair of softening and hardening response jumps can be clearly observed. Also, the presence of backlash lowers the resonance frequency compared to the LTV predictions. In Fig. 12(c) in which both types of nonlinearities exist, their interaction appears to increase the frequency region between response jump up and down. For heavily loaded condition, the dynamic response essentially produces the same trends as shown in Fig. 12(d–f). From these results, it is clear that although mesh stiffness asymmetry affects response amplitude and resonance frequency, its effect is not as strong as backlash nonlinearity, and furthermore the response jump discontinuity is obviously caused by backlash. Also, mesh stiffness asymmetry has slightly more effect on dynamic response in light load condition as compared to heavy load one.

5. Concluding remarks

A nonlinear time-varying dynamic model of a hypoid gear pair system with time-dependent mesh point, line-of-action vectors, asymmetric mesh stiffness, mesh damping and backlash nonlinearities is formulated to

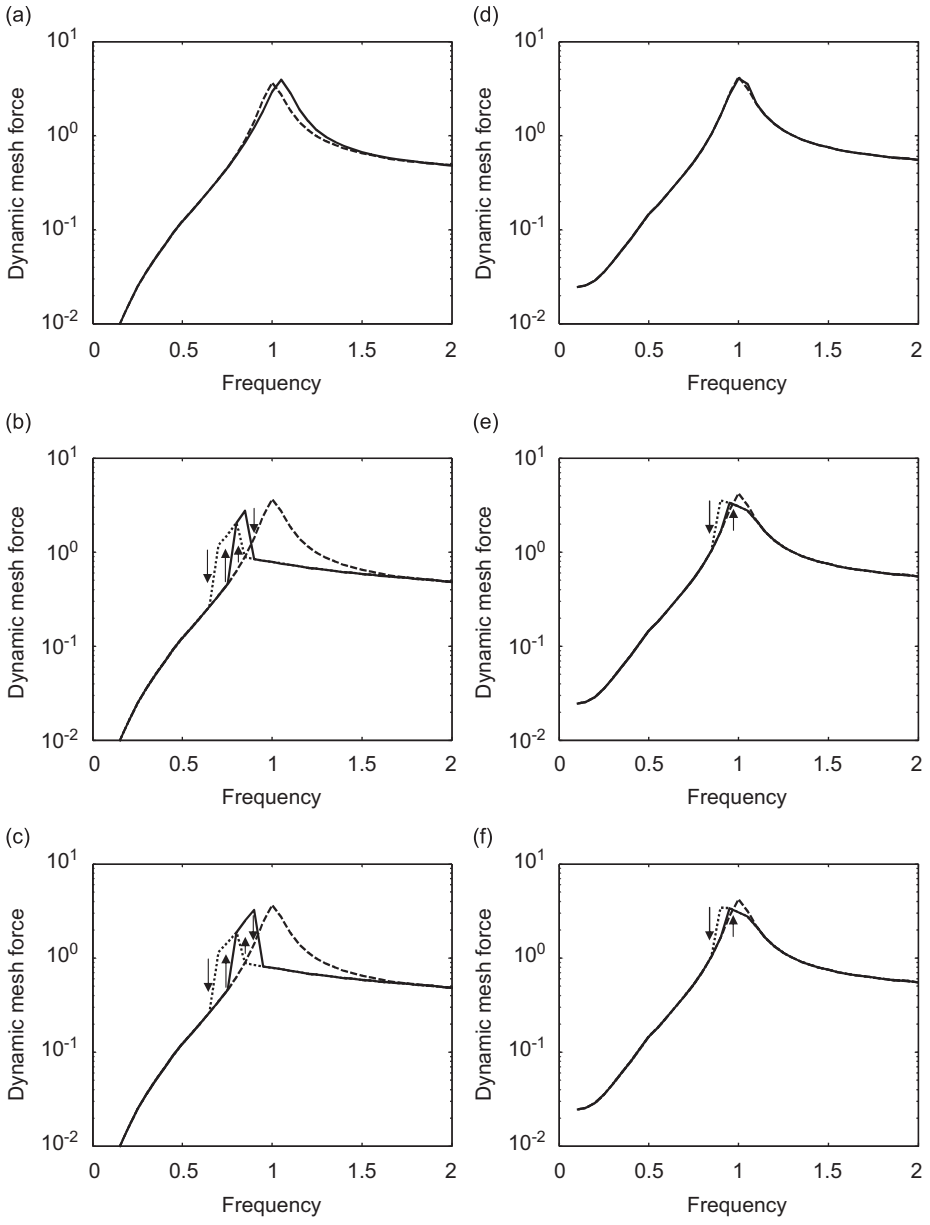

Fig. 12. Dimensionless dynamic mesh force $\tilde{F}_m$ versus dimensionless frequency $\tilde{\omega}$ for different dynamic models. Light load $\tilde{T}_p = 0.4$, (a) only mesh stiffness asymmetry without backlash, (b) only backlash without mesh stiffness asymmetry, (c) with both mesh stiffness asymmetry and backlash. Heavy load $\tilde{T}_p = 2.01$, (d) only mesh stiffness asymmetry without backlash, (e) only backlash without mesh stiffness asymmetry, (f) with both mesh stiffness asymmetry and backlash. ———, nonlinear time-varying model (increasing frequency); · · · · · · · · · · · ·, nonlinear time-varying model (decreasing frequency); - - - -, linear time-varying model.

study the effect of mesh stiffness asymmetry on dynamic response. Using this model, the effects of asymmetric mesh stiffness parameters, such as mean mesh stiffness ratio, mesh stiffness variation and mesh stiffness phase angle on the dynamic mesh force response and tooth impact regions are examined. It is obvious that mesh stiffness asymmetry does affect hypoid gear dynamic response considerably. The increase of mean mesh stiffness ratio r_k tends to worsen dynamic response especially for lightly loaded case. The increase of mesh stiffness variation $\tilde{k}_{1a1}$ and $\tilde{k}_{2a1}$ will aggravate dynamics significantly especially for heavy load case. Also, $\tilde{k}_{1a1}$ affects dynamic response more than $\tilde{k}_{2a1}$ especially for heavily loaded case. The effects of mesh stiffness phase angle ϕ_{k11} and ϕ_{k21} on dynamics depend on the values of $\tilde{k}_{1a1}$ and $\tilde{k}_{2a1}$. When $\tilde{k}_{1a1}$ and $\tilde{k}_{2a1}$ are negligible, ϕ_{k11}

and ϕ_{k21} have no effect on dynamic response at all. When $\tilde{k}_{1a1}$ and $\tilde{k}_{2a1}$ are very small (less than 0.05), ϕ_{k11} and ϕ_{k21} have only a small effect on dynamics. When $\tilde{k}_{1a1}$ and $\tilde{k}_{2a1}$ are large enough, it is shown that both ϕ_{k11} and ϕ_{k21} affect dynamics with ϕ_{k11} influencing the response more than ϕ_{k21}. Furthermore, only double-sided tooth impact region is affected by r_k, $\tilde{k}_{2a1}$ and ϕ_{k21}, while single-sided tooth impact and no impact regions change very little. This is because these parameters will take effect only if double-sided tooth impact condition is satisfied as shown in the theoretical formulation.

Dynamic models with only mesh stiffness asymmetry, with only backlash and with both mesh stiffness asymmetry and backlash are also analyzed and compared. The results show that although mesh stiffness asymmetry affects dynamic mesh force amplitude and resonance frequency, its effect is not as prominent as backlash nonlinearity, and the response jump discontinuity seen is mostly caused by backlash. Mesh stiffness asymmetry nonlinearity has more effect on dynamic response for lightly loaded condition as compared to heavily loaded one.

References

[1] R.J. Comparin, R. Singh, Non-linear frequency response characteristics of an impact gear, *Journal of Sound and Vibration* 134 (1989) 259–290.
[2] A. Kahraman, R. Singh, Non-linear dynamics of a spur gear pair, *Journal of Sound and Vibration* 142 (1990) 49–75.
[3] A. Kahraman, R. Singh, Non-linear dynamics of a geared-rotor bearing system with multiple clearances, *Journal of Sound and Vibration* 144 (1991) 469–506.
[4] A. Kahraman, R. Singh, Interactions between time-varying mesh stiffness and clearance non-linearities in a geared system, *Journal of Sound and Vibration* 146 (1991) 135–156.
[5] Y. Cheng, T.C. Lim, Dynamics of hypoid gear transmission with nonlinear time-varying mesh characteristics, *Journal of Mechanical Design* 125 (2003) 373–382.
[6] J.D. Smith, *Gear Noise and Vibration*, second ed., Marcel Dekker, New York, 2003.
[7] P. Velex, M. Maatar, A mathematical model for analyzing the influence of shape deviations and mounting errors on gear dynamic behavior, *Journal of Sound and Vibration* 191 (1996) 629–660.
[8] S. Vijayakar, *Contact Analysis Program Package: Calyx*, Advanced Numerical Solutions, Hilliard, OH, 2003.
[9] J. Wang, T.C. Lim, M. Li, Dynamics of a hypoid gear pair considering the effects of time-varying mesh parameters and backlash non-linearity, *Journal of Sound and Vibration* 308 (2007) 302–329.
[10] MATLAB Version 7.0.1. (R14) Service Pack 1, The MathWorks, Inc., 2004.